UNIVERSITY of CALIFORNIA
SANTA CRUZ

INVESTIGATION OF LOCAL STRUCTURE OF NOVEL MATERIALS USING EXAFS TECHNIQUE

A thesis submitted in partial satisfaction of the
requirements for the degree of

BACHELOR OF SCIENCE

in

PHYSICS

by

Michael Edmund Joseph Kozina

June 2010

The thesis of Michael Edmund Joseph Kozina is approved by:

Professor Frank G. Bridges Advisor	Professor David P. Belanger Senior Theses Coordinator

Professor David P. Belanger
Chair, Department of Physics

Abstract

Investigation of Local Structure of Novel Materials using EXAFS Technique

by

Michael Edmund Joseph Kozina

The Extended X-ray Absorption Fine Structure (EXAFS) technique was used to examine the local properties of several novel materials. The EXAFS technique involves measuring the transmission of x-rays through materials (or, alternatively, the emitted x-ray fluorescence of materials) and examining the deviations of the absorption coefficient from the embedded atom model as a function of energy. This provides a probe of local structure. We use this probe to study two materials in detail: ZnS:Cu,Mn,Cl and $Ba_8Ga_{16}Sn_{30}$.

ZnS:Cu,Mn,Cl is an electroluminescent phosphor. We found that device performance declined when the phosphor powder was ground finer than the manufacturer's product. We used the EXAFS technique on these ground particles and found that the Zn (host) and Mn (dopant) local structures did not appreciably change whereas the Cu (dopant) local structure did. A possible explanation for the poor device performance is that the device is cleaving along either the CuS-ZnS boundary or through the CuS (both in (111) direction) and exposing CuS sites (where electroluminescence occurs) to the surface. This leads to fewer trapped states and a weaker local electric field enhancement.

For $Ba_8Ga_{16}Sn_{30}$ and other Type I clathrates, past experiments have only been

able to suggest that Ga-Ga bonds are not favored in the cage structure. We provide definitive evidence that this is indeed the case. Using the EXAFS technique, we compare the EXAFS signal for our sample with theoretical Ga-Ga and Ga-Sn standards. We find that only $\sim 15\%$ of Ga neighbors are Ga, fewer than randomness predicts. We use this result along with diffraction data on occupational parameters to propose a possible structure for the unit cell. Additionally, we find significant disorder in the Ga/Sn cage lattice; the Ga-Sn bond is 0.07Å and the Ga-Ga 0.2Å shorter than the average bond length, which must contribute to the smaller thermal conductivity exhibited by this compound.

Contents

List of Figures

List of Tables

For Edmund Mockus. We are together.

Acknowledgements

Out of fear of forgeting someone I am reluctant to list all those to whom I am indebted. However, there are certain people whom justice demand be mentioned.

My parents Sheila and Frank Kozina have supported me throughout my life, despite the grief I have brought on them. My sisters Dorothy and Ellen have put up with me, and patiently listened when I was so eager to explain some physical concept to them. My grandparents Edmund and Louise Mockus have sheltered me (literally) for the past three years, and it has been a blessing to spend so much time getting to know them.

I have been graced to be a part of the UC Santa Cruz Newman Catholic group since I was a freshman. To the leaders of Newman, Br. David Betz, Sr. Maryann Cantlon, Fr. James Graham, and Fr. Rodolfo Contreas, I offer much thanks. Also, mention must be made to all of my friends at Newman, especially my fellow Newman Bad Boys, Jason Nguyen, Ericks Celis, Andrew Iraheta, and Kevin Garcia (author of the title "Newman Bad Boys").

The many physics, mathematics, and classics professors under whom I have had the pleasure of studying are also due much thanks. While so many of these instructors where critical in my education, there are several who deserve special mention.

Of the physicists, Peter Young's handouts were invaluable, and I always found his classes very straightforward. Zack Schlesinger's unique teaching style initially aggravated me, until I realized the value of thinking for oneself in physics. Two professors I must include together, because I have never had more challenging physics

instructors than these: Howie Haber and Onuttom Narayan. While their courses were significantly more difficult than others, I feel like I learned an incredible amount. Last (of the physicists) I thank Jason Nielsen for innumerable off-topic conversations, limited to but not excluding the intricacies of basketball.

In the classics department, two figures stand out: Tom Walsh and Gildas Hamel. Tom was one of the most benign characters I have met at Santa Cruz, but his instruction did not suffer for it and rather was enhanced. Gildas is probably the most personable man I have met, as well as incredibly interesting. I will never forget that on our last day of instruction he made the class a French dessert, wrote the recipe on the board (in metric units, naturally), and told us his intriguing life story.

Finally, we reach the math department. Marty Weissman was the instructor for my first upper division math course. His interest in the success of the student, as well as his novel, interactive teaching style, are invaluable qualities in any professor. Mention must also be given to Michail Zhitomirskii, the visiting professor from Technion in Israel. It would be a crime to forget his frank humor and bizarre analogies. Because of him, I will make sure never to drop an egg on the kitchen floor, lest my future wife leave me.

Last, I cannot fail to thank Richard Mitchell. From the very start of my career at Santa Cruz, he has been an excellent instructor and friend. His amazing lectures were a pleasure to attend, and I hope many future Santa Cruz students will have the chance to study under him.

The graduate students and post-docs with whom I have been working—especially

Justin Jiang, Chris France, Scott Medling, Ben Balaban, and Carley Corrado—all have been very gracious and helpful, especially when I was first learning lab protocol.

My adivsor Bud Bridges has been extremely helpful and thoughtful over the past two years. He has been willing to give advice not only on research but also on my coursework, and he has exposed me to many opportunities in science I would not have enjoyed without him. His patience with me has been incredible—seriously, I cannot believe that he has yet to give up on me, for he has had to repeat so many things to me. It has been a true blessing to work with and know Bud.

1

Introduction

Zinc Sulfide doped with Copper, Manganese and Chlorine (ZnS:Cu,Mn,Cl) and the type I clathrate $Ba_8Ga_{16}Sn_{30}$ are two compounds with drastically different macroscopic properties. In this thesis, however, an attempt will be made to show that there is a fundamental connecting link between these materials. It is the local structure—that is, the environment very close to each atom—that helps explain the global properties enjoyed by ZnS:Cu,Mn,Cl and $Ba_8Ga_{16}Sn_{30}$.

The substance ZnS:Cu,Mn,Cl has been known as a phosphorescent material for over a century. When light shines on ZnS:Cu,Cl,Mn, it glows. Moreover, the material is electroluminescent; that is, under an applied electric field, the material also emits light. Clearly, the applications for a novel type of lightsource are vast. It is of great practical interest, then, to study the electroluminescent process in ZnS:Cu,Mn,Cl.

We have made electroluminescent devices out of ZnS:Cu,Mn,Cl. Note that we have also made devices with ZnS:Cu,Cl, which emit light at a different peak frequency than

those made with ZnS doped with Mn as well as Cu and Cl. However, in the present work we concern ourselves only with ZnS:Cu,Mn,Cl.

The phosphor devices can be treated like capacitors, namely that the potential difference V across a device made with ZnS:Cu,Mn,Cl results in an electric field E of magnitude V/d, where d is the thickness of the device. Moreover, there is a requisite electric field strength needed for devices to electroluminesce (EL). To make devices more useful in applications, a smaller voltage is required. Thus, it is necessary to make the device very thin so that the electric field is sufficiently high for a low applied voltage.

Our collaborators attempted to make thin devices by grinding ZnS:Cu,Mn,Cl powders. However, they found that the grinding, while allowing for thinner devices, inhibited the electroluminescence. Something was damaged in the device, and they were uncertain what was damaged. This is where the power of the EXAFS technique is made manifest.

The Extended X-ray Absorption Fine Structure (EXAFS) technique has the ability to probe the local environment about different atoms. When x-rays of energy near the absorption edge of an atom are incident on a material, electrons are expelled from the atoms and backscatter off neighboring atoms. This backscattering affects the ability of the atom to absorb photons, and we can use this to discover the structure of the atoms in the immediate vicinity.

Using EXAFS, we were able to probe the local structure of Zn, Mn, and Cu in the phosphor. This experiment is important because it is the local structure that offers

insight into why the ground phosphor failed to EL. Below we explain in detail how the EXAFS technique provided a window into explaining the failure of the device through revealing the local structure about Mn, Zn, and Cu.

Thermoelectrics are another class of materials that are intensely interesting because they have the ability to transform a difference in temperature into a difference in electric potential, and vice versa. That is, if one end of a thermoelectric is at a higher temperature than the other, electricity is generated. Or, if a current flows through the thermoelectric, one end becomes cool and the other hot. There is active research in thermoelectrics into applications for both transforming waste heat into electricity and creating refrigerators with no moving parts, controlled by the applied current alone.

The quality thermoelectric is given by the dimensionless figure of merit ZT, where T is the temperature in Kelvin and Z is a combination of three physical properties important in thermoelectric processes: the Seebeck coefficient S (ratio of voltage difference to temperature difference), the thermal conductivity κ (ability to transport thermal energy), and the electrical conductivity σ (ability to transport electons). Specifically, $ZT = S^2\sigma/\kappa$.

One thermoelectric, the the type I clathrate $Ba_8Ga_{16}Sn_{30}$, is particularly interesting because it has a lower thermal conductivity than other compounds very close to it in structure (like $Ba_8Ga_{16}Ge_{30}$). Like other clathrates, $Ba_8Ga_{16}Sn_{30}$ has a cage composed Ga and Sn atoms surrounding a Ba atom. The rattling of the Ba atom can scatter low frequency phonons (heat waves), and inhibit the thermal conductivity.

However, while this process exists in most clathrates, $Ba_8Ga_{16}Ge_{30}$ still exhibits a comparatively low thermal conductivity. The question remains why this is so.

It is important that a thermoelectric have a low thermal conductivity (in order to increase the figure of merit), and so it is imperative that we gain insight into the transport properties of this material. As in the example of the electroluminescent ZnS:Cu,Mn,Cl devices, EXAFS is a useful tool for studying the thermoelectric $Ba_8Ga_{16}Sn_{30}$. As explained more thoroughly below, we were able to use EXAFS to explore the local structure about Ga and Sn and provide a partial explanation why the thermal conductivity of this clathrate is lower than similar compounds.

For both ZnS:Cu,Mn and $Ba_8Ga_{16}Sn_{30}$, the central idea behind our research is to examine the local structure in hopes of explaining bulk properties. Ultimately, the EXAFS technique can only yield information about atoms that are very close to each other, as opposed to long-range techniques. However, exploring local structure with EXAFS gives insight into properties of macroscopic materials which cannot be discovered using other means. Therefore, the EXAFS technique is well-suited for investigating certain material properties.

In the following chapters, I will first explain the physics behind the EXAFS technique and our methods for analyzing EXAFS data. After I will talk about the research performed on ZnS:Cu,Mn,Cl using EXAFS. Last I will discuss our findings for $Ba_8Ga_{16}Sn_{30}$.

2

The Physics behind EXAFS

The EXAFS technique is a way to gather information about the local structure about an atom based upon the scattering of ejected electrons. In order to better understand this process, it is useful to examine the idea of absorption.

When an oscillating electromagnetic field is incident on an atom, there is a probability that an electron of the atom will be excited and leave the atom. Specifically, when a quantum of this electromagnetic radiation (a photon) with sufficient energy strikes the atom, an electron can be released. The incoming photon must have enough energy to excite an electron from its bound state in the atom to a free state able to move through the nearby space. If the magnitude of the energy of the bound state is E_0, then the incident photon must have energy greater than E_0 to eject the electron.

When an electron is ejected by an incident photon of energy E, it becomes a photoelectron with energy $E - E_0$ and propagates away from the atom of origin as a spherical wave. Because of the wave nature of the photoelectron, a variable more

natural for characterizing the photoelectron than its kinetic energy is its wave vector, k. Since the electron can be treated as a free electron, it has energy:

$$E - E_0 = \frac{\hbar^2 k^2}{2m}, \tag{2.1}$$

where m is the electron's mass. We can invert this expression to find k as a function of E, yielding:

$$k = \frac{\sqrt{2m(E - E_0)}}{\hbar}. \tag{2.2}$$

For EXAFS studies, typically core electrons are excited, either an electron from the K shell or the L_I, L_{II}, or L_{III} shells. The resultant electron wave then interacts with atoms close to the central atom and scatters off of them. This scattering occurs in all directions. However, the only direction of interest is that directed back towards the central atom (known as backscattering). When the electron leaves a core hole in the central atom, the state left is very small, and so only the scattering in the π direction has any significance at the center atom. As the scattered wave approaches the central atom, it interferes with the outgoing electron wave, and this interaction between the emitted and backscattered electron waves affects the absorption of photons by the central atom.

Let the absorption coefficient of photons by the central atom be given by μ_0. Here we are making an assumption that μ_0 would be the absorption of the atom if it were surrounded by the average potential of its neighbors arranged randomly. Therefore,

μ_0 does not include any point scattering effects, which would contribute to the EXAFS signal. This approximation is known as the embedded atom aproximation.

When other atoms are present, backscattering of the electron off the neighbors occurs, and the absorption is modified. Specifically, the absorption coefficient is given by $\mu = \mu_0(1 + \chi(k))$, where $\chi(k)$ is a unitless function known as the EXAFS function dependent on the wave vector k of the photoelectron. The EXAFS function represents the deviation of the absorption, known as fine structure. It is given by[4]:

$$\chi(E) = \sum_j N_j S_0^2(k) F_j(k) e^{-2\sigma_j^2 k^2} e^{-2r_j/\lambda(k)} \frac{\sin[2kr_j + 2\delta_1(k) + \theta_j(k)]}{kr_j^2}. \tag{2.3}$$

Here N_j is the number of neighboring atoms of type j and $F_j(k)$ is the scattering amplitude of the photoelectron with wave vector k off of atom type j.

We assume a harmonic thermal vibration of the atoms about their equilibria. Because the lifetime of the core state is so brief ($\sim 10^{-15}s$[4]), the ejected photoelectron essentially sees a snapshot of the neighboring atoms; that is, to the photoelectron, the neighbors are stationary. However, because of thermal vibration, the location of the neighbors relative to the central atom follows a particular distribution. Because we are assuming harmonic motion, we have a Gaussian distribution for this thermal disorder. In the EXAFS equation, this correction is accounted for by the correlated Debye-Waller factor σ_j and the Gaussian term $e^{-2\sigma_j^2 k^2}$.

The phase shift experienced by the photoelectron has two components, aside from the $2kr_j$ (since it goes out r_j and returns r_j): $2\delta_1(k)$ is the phase shift caused by

the central atom, and is doubled because the photoelectron sees this potential twice (leaving and returning); $\theta_j(k)$ is the phase shift from the jth neighbor, whose potential the photoelectron experiences only once.

There are also losses due to inelastic interactions. At the center atom, there can be losses due to multiple excitations, here taken into account by the factor S_0^2, which is roughly (but typically slightly less than) unity. The $e^{-2r_j/\lambda(k)}$ term models the reduction in amplitude of the EXAFS signal due to inelastic scattering; here $\lambda(k)$ is the inelastic mean free path of the electron, and r_j is the distance from the center atom to the neighboring atom in question. Note that the argument of the exponential is twice r_j because the path goes away from the center atom and back again.

Thus, when electromagnetic radiation of sufficient energy is incident on a compound, electrons from atomic cores are ejected. The ejected electron from one atom, permeating the space about the central atom as a photoelectron wave, scatters off neighboring atoms. Some of this scattering is directed immediately back towards the central atom, and this backscattering interferes with the part of the wave leaving the atom. The interference of the outgoing and returning photoelectron wave modulates the absoprtion coefficient of the central atom. That is, the central atom's ability to absorp radiation is affected by this interference. The deviations of the absorption coefficient from the embedded atom value (the fine structure) can be analyzed to determine the local structure about the central atom. This is the heart of EXAFS analysis.

3

EXAFS Data Collection and Analysis

3.1 Data Collection

EXAFS data are collected in primarily two ways: transmission and fluorescence. In a nutshell, transmission data directly measure the absorption coefficient of the sample as a function of energy using detectors that record the amount of radiation entering and passing through the sample. On the other hand, energy dispersive detectors counting the photons emitted by the sample under incident x-ray radiation collect fluorescence data. For the research presented in this thesis, the transmission method was much more frequently employed, and so this method will be explained in further detail.

In order to probe samples using x-rays, a source of these x-rays is needed. Typ-

ically, the x-rays are generated at a synchrotron. In the synchrotron, electrons are forced to move in a curved loop by means of magnets. When the electrons move along the path, their direction of motion changes, and so they accelerate. Charges that are accelerated give off radiation. This radiation is what is directed at the sample. The data presented here were gathered at the Stanford Synchrotron Radiation Lightsource (SSRL), a part of the SLAC National Laboratory.

When the radiation emanates from the electron beam, it is composed of a range of energies. However, for EXAFS results, one wants a narrow band of energy, so that the absorption coefficient can be measured as a function of energy accurately. In order to reduce the range of energies in the radiation, a double crystal monochromator is placed in the path of the x-rays. The x-rays Bragg scatter off the first crystal in a certain direction, depending on the wavelength and hence the energy of the incoming photons. The second crystal plane is initially parallel to the first, causing only a very small range of energies to be Bragg scattered in the direction towards the sample. Then, in a process known as detuning, a very slight relative angle is introduced between the two crystal planes. This helps to remove harmonics, which can reduce the EXAFS signal. The energy of the radiation incident on the sample is then scanned by rotating the crystal planes in relation to the beam. Additionally, better energy resolution can be achieved by reducing the vertical width of the beam using moveable slits. (For our experiments, the vertical slits were separated by ~ 0.3 to 0.6mm.)

We choose an energy range dependent on the type of element we are probing.

Specifically, the fine structure in the absorption coefficient (that is, EXAFS) is only present in a small energy range just above the absorption edge energy. The absorption edges typically correspond to either the K- or L-shell. (Recall that the K-shell is the innermost shell of electrons, made up of the two 1s states, whereas the L-shell contains the 2s and 2p states.) For most elements that we probe, the absorption energy for the core state is about 5-30keV.

At the beamline at SSRL where we performed our experiments, there were two choices of crystal alignments for the monochromator: (111) and (220). The two crystals are suited for different purposes. For example, crystals in the (111) direction are ideal for Copper in ZnS. Recall that Cu and Zn are neighbors in the periodic table, and so the absorption energy for the Cu K-edge is just below that for Zn K-edge. Therefore, when exciting Cu in a compound with Zn as well, there is danger of exciting some of the Zn as well. The (111) crystals do not have the second harmonic, which is at the right energy to excite Zn, while (220) crystals do. Thus the (111) crystals are used for Cu K-edge in a compound with Zn. On the other hand, Barium K-edge ($\sim$ 37keV) requires the (220) direction, for the (111) crystals only work up to $\sim$ 19keV.

Once we have a beam of x-ray radiation narrowly ranged about our desired energy, we send it through a series of detectors and samples to measure the absorption of x-rays as a function of energy. First, the beam goes through a baseline detector (known as I_0), used to characterize the incoming radiation. Then, the beam passes through the sample, where it is partially absorbed. Those photons not absorped

by the sample pass through a second detector, I_1. After I_1 the remaining photons go through a reference sample (typically a foil corresponding to the element we are currently probing). Last the part of the beam not absorbed by the reference goes into another detector, I_2.

In order to understand how the data collected by the detectors can reveal the absorption coefficient of the material, a little explanation is required. For most materials, absorption of incident radiation can be modeled as an exponential drop-off, with a characteristic length scale $1/\mu$, where μ is the absorption coefficient (and is generally a function of the energy of the radiation absorbed). Specifically, we have:

$$I_{\text{trans}} = I_{\text{in}} e^{-\mu x}, \tag{3.1}$$

where I_{trans} is the intensity of the radiation transmitted through the material, I_{in} is the intensity of the incident radiation, x is how far into the sample the beam permeates (for our purposes x is the thickness of the sample), and μ is the energy-dependent absorption coefficient.

It is a relatively simple matter to solve for the absorption coefficient using Eq. 3.1, yielding:

$$\mu = \frac{1}{x} \log \frac{I_{\text{in}}}{I_{\text{trans}}} \tag{3.2}$$

The absorption coefficient can be broken down into three pieces. First, there is a background contribution μ_b due to absorption by other atoms. This includes not

only other shells in the probed atom but also other atoms in the sample and atoms in the environment (the cryostat, the air, etc.).

The second contribution to the absorption coefficient, μ_0, is the absorption coefficient for the embedded atom approximation. In this picture, the atom is surrounded by a uniform density of atoms, thus lacking any type of regularity. Therefore, the atom feels the average potential due to its neighbors without suffering the effects of the photoelectron backscattering off the neighbors.

The final contribution to the absorption coefficient is proportional to the embedded atom absorption and represents the deviation from this approximation, namely χ. This function is known as the EXAFS function. Subtracting the background contribution μ_b from the overall absorption coefficient gives the absorption coefficient for the edge under study. Note that both μ_0 and χ are functions of the energy of the incident radiation, and so are more properly written as such (where $\mu(E)$ is the absorption coefficient less the background contribution):

$$\mu(E) = \mu_0(E)[1 + \chi(E)] \tag{3.3}$$

We can solve Eq. 3.3 for $\chi(E)$, yielding:

$$\chi(E) = \frac{\mu(E) - \mu_0(E)}{\mu_0(E)} \tag{3.4}$$

It is our goal to extract this $\chi(E)$ function from our data.

Recall from above we showed that the intensity data collected can be used to find the absorption coefficient, $\mu(E)$ by taking the natural logarithm of the ratio of the

intensities and dividing by the sample thickness. However, finding $\mu_0(E)$ requires more subtle analysis.

3.2 Data Reduction

Before we can interpret our data, we must recast the data in a form conducive to analysis. This process is known as data reduction. We begin with the region known as the pre-edge, namely the energy range before the energy of the bound electron. See Fig. 3.1 for sample data (the pre-edge region is from $\sim$ 10150eV to $\sim$ 10350eV).

For transmission data, the absorption coefficient below and above the absorption edge can be modeled as $C\lambda^3 - D\lambda^4$, known as the Victoreen formula [4], where C and D are experimentally determined constants unique to each element and different for the region above and below the edge. We can use this function to help in subtracting the contribution to the absorption coefficient caused by external agents (μ_b).

Let us now explain the specific process for subtracting the background. First, we find the best fit straight lines through the pre- and post-edge data. The difference in absorption coefficient between these two lines at the edge is known as the edge jump. Now imagine for a moment that the pre-edge data extended beyond the edge, overlapping with the energy range that forms the post-edge. The difference between the pre- and post-edge data in this region is proportional to the edge jump found earlier. The exact proportionality is calculated using the Victoreen coefficients mentioned above. We then proceed to subtract this calculated difference from the post-edge data. Ef-

fectively, we have now removed the edge jump and formed a continuous absorption coefficient.

It may be hard to see why we go through the process of subtracting the difference from the post-edge data. Our motivation is to subtract the background, which is a continuous function. However, our data have a discontinuity at the edge. It is necessary, therefore, to make the data continuous through our subtraction process described above to fit an appropriate background.

Once we have fit the background, we take the background function and subtract it from the original data. Our digression into forcing the absorption to be continuous was simply for the purpose of finding the correct background function. Once this has been achived, we restore the data set to its original form. The data with the background thus subtracted is known as the "pre-edge" data. See Fig. 3.1 for a pre-edge fit overlaid with sample data.

After the pre-edge fit, the data after the edge (the post-edge) are fit with a set of cubic splines, using typically 5-8 knots (connection points between splines). The cubic splines are not functions of the energy E directly. Rather, they are a function of E^p, where p lies between 0.5 and 1. This seemingly odd construction is in fact quite useful, because it allows for the splines to be evenly spaced in k-space as opposed to E-space. To see this, remember that $k \sim (E - E_0)^{0.5}$. Evenly spaced regions in k-space are not mapped to evenly spaced regions in E-space. This would appear to necessitate that p be 0.5. However, due to the presence of several different oscillations in the data, the power needed can vary between 0.5 and 1. Figure 3.2 sample data

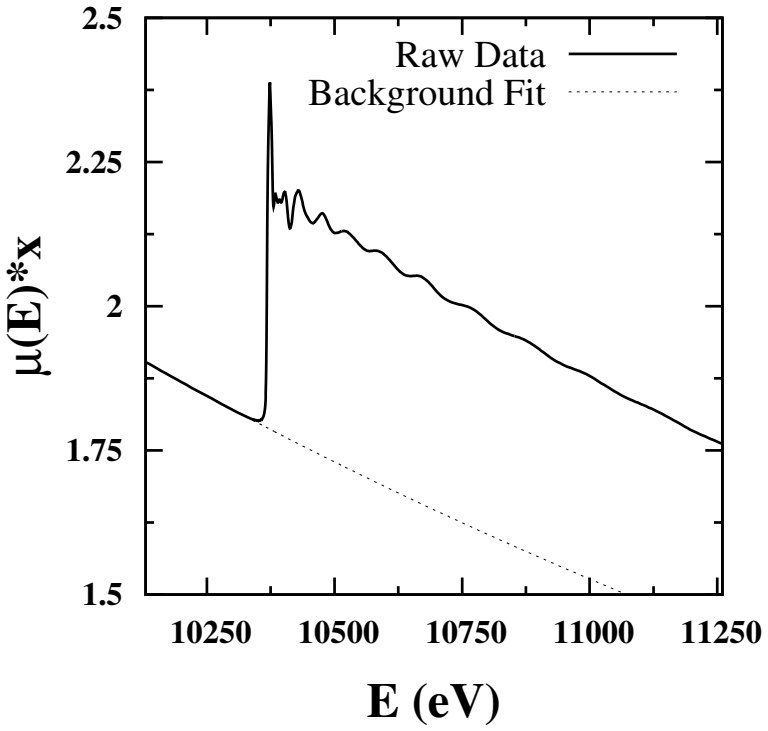

Figure 3.1: Plot of $\mu(E) * x = \log \frac{I_0}{I_1}$ versus incident x-rays (solid) and the fit to the pre-edge using the Victoreen formula (dashed) for Ga K-edge $Ba_8Ga_{16}Sn_{30}$.

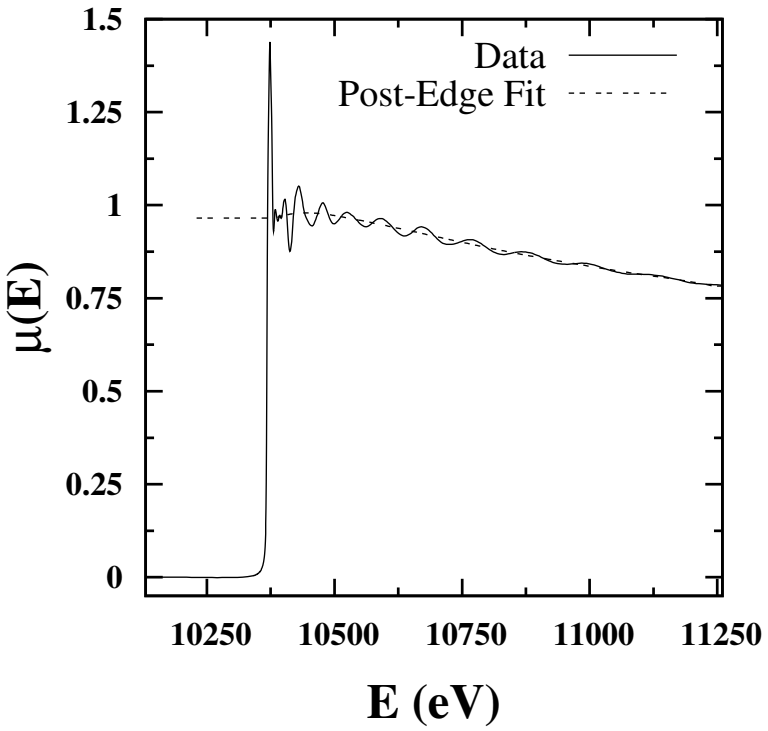

Figure 3.2: Data normalized by edge jump and pre-edge background subtracted (solid) and post-edge fit (dotted) versus incident x-ray energy for Ga K-edge in $Ba_8Ga_{16}Sn_{30}$.

with the post-edge fit are shown.

The purpose of the cubic spline fitting is to find a functional form for the contribution to the absorption coefficient due to the embedded atom, μ_0. Once we have this functional form for $\mu_0(E)$, we can evaluate $\chi(E)$ (recall Eq. 3.4), our EXAFS signal.

Recall from the previous chapter, though, that the EXAFS equation (Eq. 2.3) is calculated as a function of the photoelectron k-vector. It is therefore necessary to

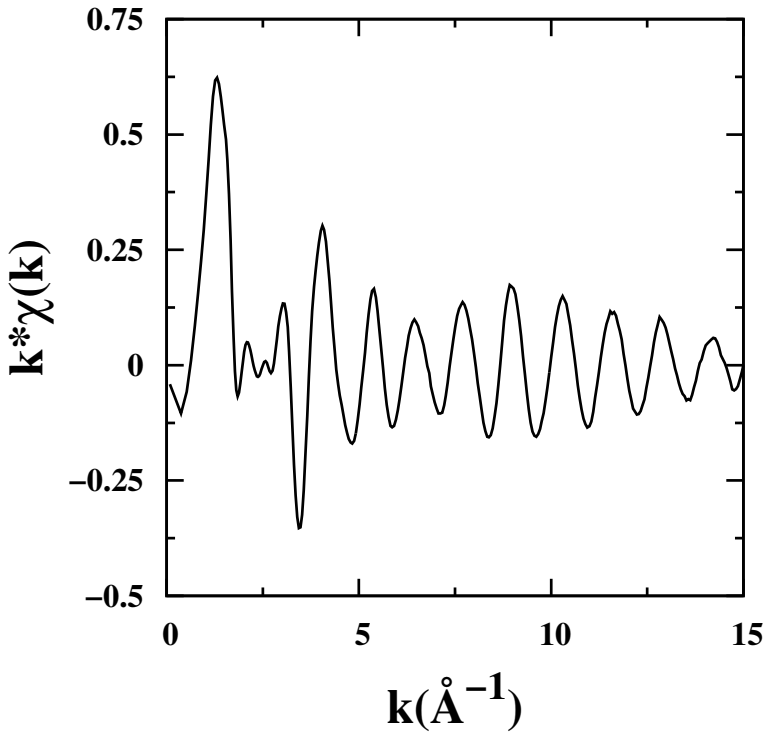

Figure 3.3: Sample k-space data for the Ga K-edge of $Ba_8Ga_{16}Sn_{30}$ at T=6K. Note that in this plot the ordinate is $k * \chi$, not χ. This helps to make the signal more uniform. (Recall the $1/k$ factor in the EXAFS equation, Eq. 2.3, which acts to suppress the signal at high k.)

transform our data from energy (E) space to k-space using Eq. 2.2. See Fig. 3.3 for a plot of sample k-space data.

Once we have the data in k-space, we apply a Fourier transform so that the data can be expressed in r-space (see Fig. 3.4). This step is both useful and necessary. First, the transformation to r-space is necessary because when we fit this reduced data to our theoretical models the fitting algorithm fits the real and imaginary parts

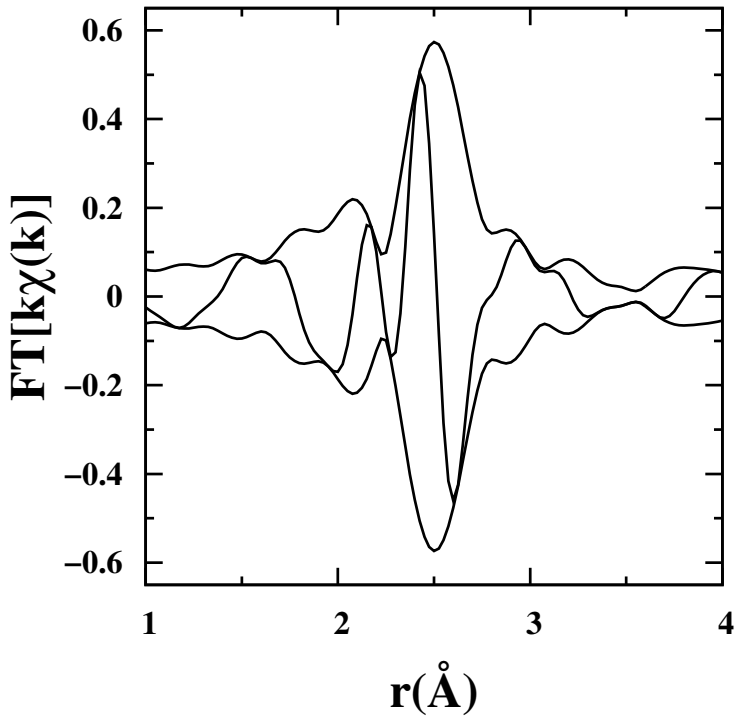

Figure 3.4: Fourier transform (FT) of k-space data for Ga K-edge in $Ba_8Ga_{16}Sn_{30}$ at T=6K, i.e. the r-space data. The FT range is 3.5-14.5Å.

of the r-space data. Second, the transformation is useful because it provides us with a more intuitive picture of the local structure. In the k-space data, different frequencies correspond to different neighbors. Therefore, because frequencies are transformed to peaks under a Fourier transform, the peaks in the r-space data correspond to different shells of neighboring atoms. We can then use this r-space data to provide a visual picture of the local structure, and to offer some direction in how we should fit the data.

It should be noted that when we Fourier transform the data, the transform is typically applied to $k\chi$, instead of χ. (In fact, $k^2\chi$ or $k^3\chi$ are sometimes used as well). We do this because the peaks in r-space under a Fourier transform are sharpest when the amplitude of the k-space data to be transformed is uniform. However, the EXAFS signal exhibits $1/k$ behavior and so the amplitude at higher k values is suppressed. By transforming $k\chi$ instead, this effect is partially mitigated (there are other factors that decrease the amplitude at higher k). In some cases, $k^2\chi$ or $k^3\chi$ are used because the backscattering amplitude can vary as $1/k^2$ instead of $1/k$.

The above steps outline the basics of the data reduction procedure. To summarize, we first take the raw data (the absorption coefficient versus energy) and subtract the background due to external atoms in the pre-edge fit. Next, we determine the contribution due to the embedded atom (μ_0) using a post-edge fit. Third, we map the energy-space data into k-space under the transformation given by Eq. 2.2. Last, we apply a Fourier transform to the k-space data so that we have a more useful representation of the data in r-space.

3.3 Data Fitting

While certain physical results can be obtained from the reduced data without further analysis (see our ZnS:Cu experiments below for an example), it is often useful to fit the data to theoretical models so that a clearer picture of the sample's local structure may be obtained.

Several decades ago, the theory behind EXAFS was insufficiently robust to be able to accurately simulate the EXAFS function for the interaction between a specific pair of atoms. It was necessary to compare data to experimental standards, namely EXAFS data for compounds whose local structures were well understood through other means. Moreover, to explore compounds with pairs of atoms for which experimental standards did not exist, certain techniques were developed to relate these atom pairs with existing experimental standards for similar atom pairs. However, the theory of EXAFS is now sufficiently accurate to calculate excellent theoretical standards for many atom pairs using the program FEFF created by John Rehr [5].

A theoretical standard is the calculated EXAFS signal for the interaction between the core atom and a specific neighbor. This standard represents what the EXAFS signal would be for a particular core atom - neighbor pair, and it lacks any thermal broadening. The program FEFF was used in our data analysis to calculate theoretical standards. See Fig. 3.5 for a sample of a theoretical standard for the Zn-S pair in ZnS at the Zn K-edge.

We fit the data using a set of theoretical standards, one for each type of neighbor for the edge atom studied. We also include standards for electrons scattering off multiple neighbors (for example, the photoelectron leaves the core, bounces off neighbor 1, then bounces off neighbor 2, and finally returns to the core atom). Linear combinations of the standards are varied with fitting software (from the RSXAP package [6]) to obtain the best fit.

There are 4 parameters for each standard that can be varied to create the best

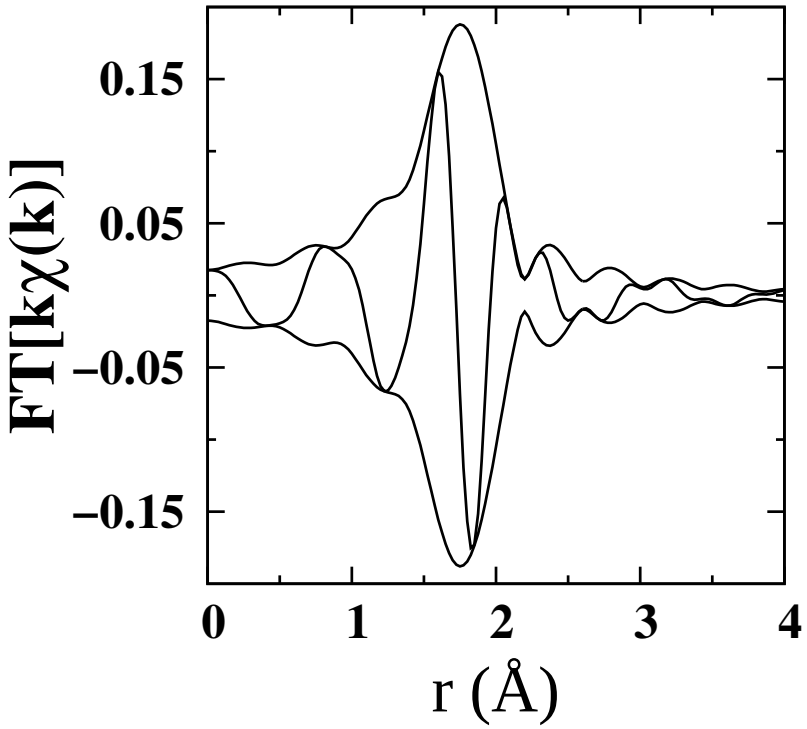

Figure 3.5: EXAFS theoretical standard in r-space for the Zn-S pair calculated using FEFF. This is the standard with Zn as the core atom and S as the neighbor. No thermal broadening is included in this standard. The envelope function is the magnitude of the Fourier transform and the oscillation is the real part.

fit. One parameter is σ, the width of the pair distribution function (PDF). This parameter is a measure of the distribution of bond lengths for a given pair of atoms. Specifically, a large σ means that there is a large variation in the separation between the core atom and the neighbor. On the other hand, a small σ signifies that there is little variation in the separation between the atoms. The temperature dependence of σ can give insight into the strength of interaction of the corresponding atom pair. This is typically calculated by performing either a correlated Debye or Einstein fit (depending on the system) to σ^2 as a function of temperature.

The fit also varies the average separation r between a pair of atoms. Specifically, $r = r_0 + \Delta r$, where r_0 is the average pair distance (typically given from diffraction) and Δr is the deviation of the pair separation from the diffraction value. It is important to allow Δr to vary because in many compounds the spacing between neighbors is not necessarily that found on average by diffraction. By allowing this deviation to be non-zero and to vary, we can measure accurately the separation between the core atom and a neighbor with accuracies of ~ 0.01 Å.

A third parameter varied by our fit is the amplitude of the theoretical standard. This parameter allows for different occupancies on sites than the crystal structure suggests. There are numerous cases where it is necessary that the amplitude of the theoretical standard be altered to fit the data. For example, some compounds can have occupancies of certain sites split between different atoms, but standards are calculated as if there were total occupancy by only one type of atom. In fitting, the amplitude of a standard is proportional to the number of that kind of neighbor. That

is, we can write the amplitude as $N * S_0^2$, where N is the number of neighbors and S_0^2 is a correction factor for multi-electron excitations as explained in the previous chapter. The constant S_0^2 is typically close to unity.

Last the fitting parameter modifies E_0, the edge energy, for each of the theoretical standards. It is necessary to allow E_0 to shift because the value chosen in data reduction, while consistent, is somewhat arbitrary. It is difficult to accurately determine the minimum energy required to eject the electron (when the photoelectron wave has $k = 0$), though it is known to be roughly within $\sim$ 10eV of the edge at the edge half-height [4]. Therefore, it is necessary that this parameter be allowed to vary when theoretical standards are being fit to the actual data. Note that the error in E_0 and Δr are correlated. For a rough approximation, one can assume an error of $0.01\mathring{A}$ in $\Delta r$for every 1eV error in E_0.

Once we have a reasonable fit to the data, we attempt to explain the macroscopic properties of the sample in terms of its local structure. This procedure necessarily varies with material, but the main idea is that local structure (small scale) can influence bulk properties (large scale).

With this in mind, let us now look at two distinct compounds: ZnS:Cu,Mn and $Ba_8Ga_{16}Sn_{30}$.

4

Studies on Ground ZnS:Cu,Mn,Cl Particles

4.1 Motivation

Apart from scientific curiosity, ZnS:Cu,Mn,Cl is an intriguing material for practical use as a solid state light source [7]. From I-V data our lab collected, we have found that our devices made with this material can be modeled as somewhat like a capacitor; thus the electric field in the device is equal to the potential divided by the device thickness. To improve device utility, it is ideal to minimize the requisite voltage for electroluminescence (EL).

However, a sufficiently strong electric field is required for EL to occur. Moreover, through several direct experiments with applied voltage and integrated intensity, we have found that increasing the peak voltage increases the EL intensity. Increasing

the voltage leads to an increase in the electric field along the CuS needles, which in turn leads to increased EL intensity.

Therefore, it is critical that device thickness be reduced, so that the electric field can remain high as the voltage drops. One proposed way to reduce device thickness is to grind up ZnS:Cu,Mn,Cl particles into smaller pieces.

When attempting to achieve EL in devices made with this finely ground material, though, our results were not ideal; devices we made with ground particles showed much reduced intensity. Thus, there must be some explanation why the devices do not work as well when made with finely ground particles than when made with the coarse factory-made particles.

It seemed that the grinding process had altered the structure of the ZnS:Cu,Mn,Cl on a local scale, rather than a global, because the material was already in a coarse powder (20-30μm) form before grinding. The EXAFS technique is a useful tool as a probe of local structure, and so we used this method to explore what was happening to the material.

4.2 Experimental Setup and Procedure

The ZnS:Cu,Mn,Cl material came as a proprietary powder from Osram-Sylvannia. The material is 5% Mn and 0.15% Cu. The fraction of Cl is unknown but presumed roughly equal to the Cu level. One of our collaborators (Chris France) made electroluminescent devices out of the powder. He mixed the powder with an organic binder

and placed the mixture in between electrical contacts. In several tests, either a sine wave voltage ($\sim$ 200V peak-to-peak with frequency ranging from 1kHz to 100kHz) or square wave voltage (same peak voltage and frequency range) was applied across the contacts, and the EL material electroluminesced.

France used material directly from the manufacturer for some tests, and also used material he ground himself. He found that grinding the particles before he used them in the device was beneficial if only very little grinding took place (particle size $\sim 10-15\mu$m). Devices made with EL powder ground more finely ($\sim 1\mu$m), however, showed a significant decrease in intensity compared to devices made with EL powder "as-is" from the manufacturer.

Because grinding particles affects their physical structure on a local scale, it seemed worthwihile to probe these ground powders using EXAFS. We looked at the EXAFS for three sets of ground particles separated by size, examining the Cu K-edge, Mn K-edge, and Zn K-edge. Note we did not look at the Cl edge because the edge energy is too low. The sizes were separated into three groups—large (20-30μm), medium (5-15μm), and small ($\sim 1\mu$m)—by suspending the particles in water and successively siphoning off the lightest particles. The sizes were verified using a microscope.

Our EXAFS samples were prepared by applying the material with a small paint-brush to the adhesive side of a piece of Scotch tape. We then took two such pieces and stuck them together, sticky sides facing each other, to create our EXAFS sample. This is known as a double layer. We then cut this sample into small strips ($\sim$ 2mm

wide) and stacked several layers together in our EXAFS sample holder, which is attached to the cryostat probe. Multiple double layers of sample were used because using too few layers results in very little absorption of the incident radiation.

The Mn K-edge and Cu K-edge EXAFS data were collected at SSRL (Stanford Synchrotron Radiation Lightsource) in fluorescence mode on beamline 10-2 using a Si 111 double monochromator. The Zn K-edge data were collected similarly but in transmission mode. The slit height was 0.7 mm, which provided an energy resolution of ∼1.3eV, and the monochromator was detuned 50% to minimize harmonics.

4.3 Results

We found interesting results in both the XANES (X-ray Absorption Near Edge Structure) as well as the EXAFS. As it has yet to be mentioned, a brief explanation of XANES is appropriate. The XANES signal is due to multi-electron events (whereas EXAFS is primarily concerned with single electron excitations) at the core atom, and adds additional structure at and in the immediate vicinity of the edge. It should be noted that at this time we are not able to model the XANES structure like we can the EXAFS, and so our analysis of the XANES must remain strictly qualitative.

For the host Zn K-edge data, the XANES remained essentially unchanged as the particle size was varied (see Fig. 4.1). This suggests that the reduction in particle size due to grinding does not affect the host sites.

Moreover, the Mn (5% dopant) K-edge data also do not show any variation in the

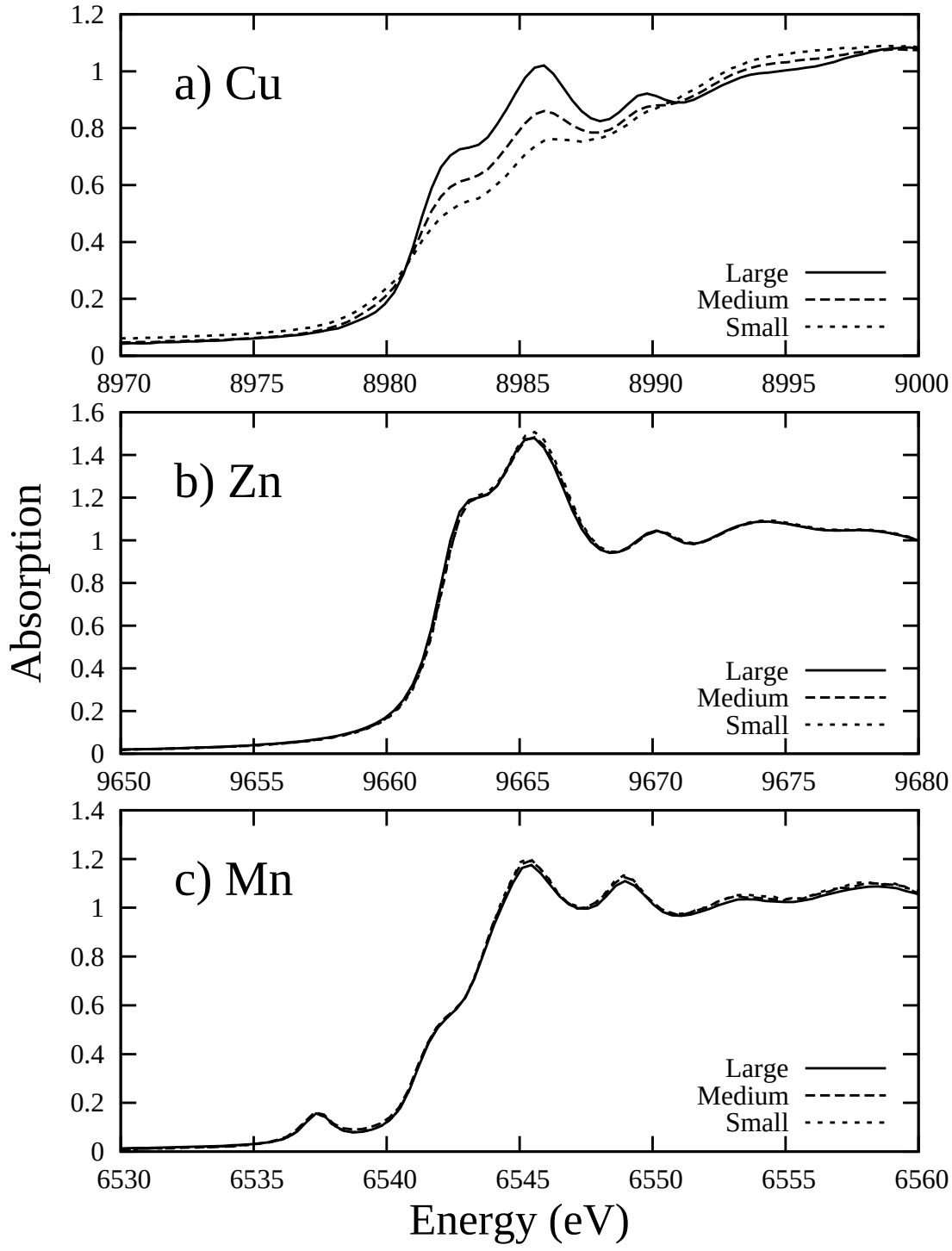

Figure 4.1: XANES data at 4K for a) Cu K-edge; b) Zn K-edge; c) Mn K-edge.

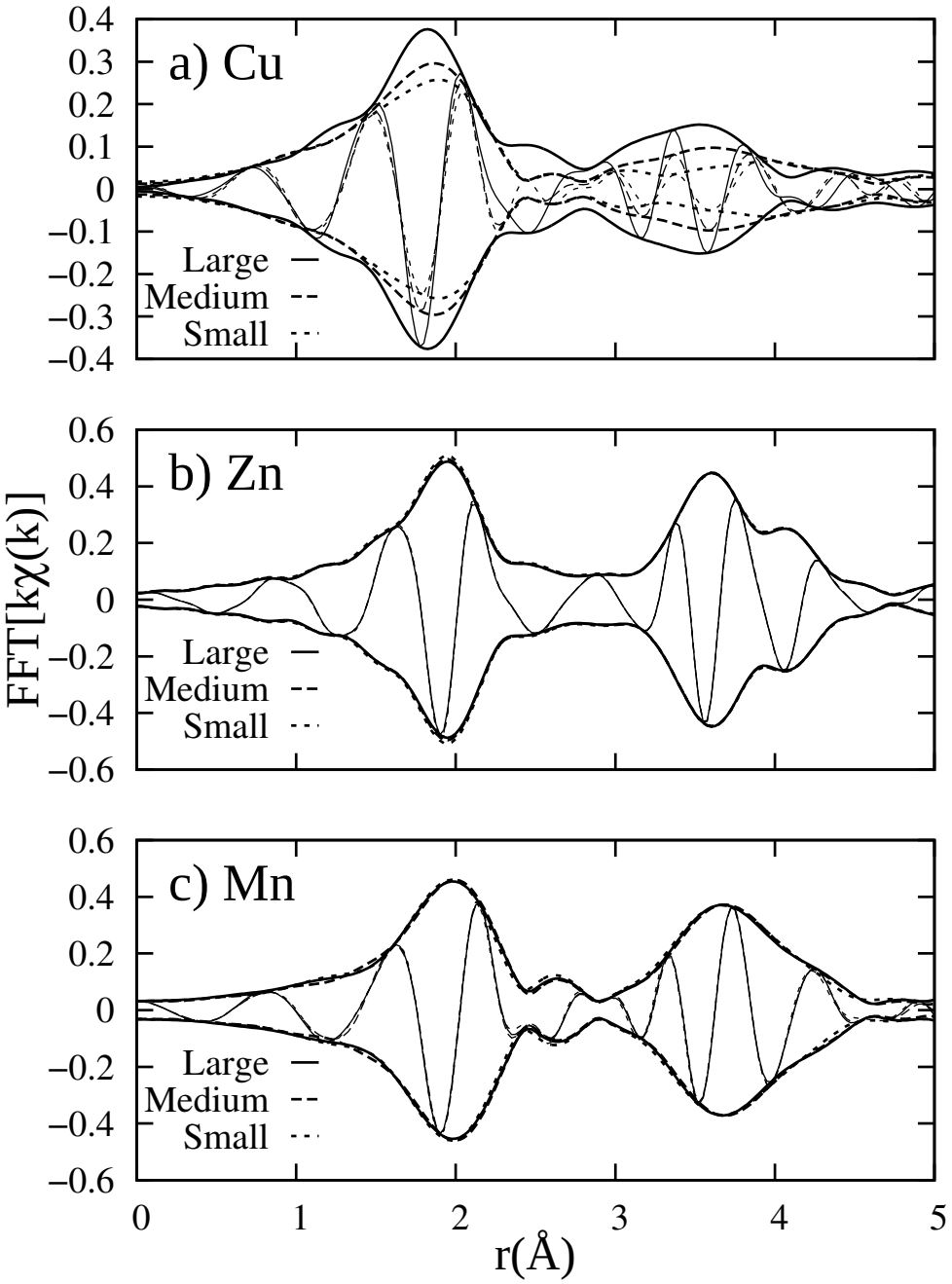

Figure 4.2: EXAFS r-space data at 4K for a) Cu K-edge (FT range 3.5-11.3Å); b) Zn K-edge (FT range 4-13.5Å); c) Mn K-edge (FT range 3.5-11Å). The oscillatory part of each plot is the real part of the Fourier transform of $k * \chi(k)$ and the envelope function is the norm of the transform. The Fourier transform range is 3-13.7Å.

XANES across particle size as well. This is to be expected, because the Mn dopant is known to substitute on the Zn host sites [8].

However, we found that the XANES data changed significantly with changing particle size for the Cu K-edge (see Fig. 4.1). In particular, as the particle size decreased, the relative height of the spike at the absorption edge dropped until it was almost no longer present.

We see similar results in the EXAFS data. See Fig. 4.2 for scans of Zn, Mn, and Cu EXAFS data in r-space. In the Zn host data, a very slight decrease in amplitude is present in the large particles compared to the small. This has been explained before [9] as due to the finite size effect of the particles, a consequence simply of the physical dimensions of particle size and not chemical composition.

On the other hand, the Cu data show distinct changes in the r-space EXAFS among the different particle sizes. For example, the data show a large reduction in peak height for the first peak as particle size drops. Along with amplitude reduction, the first peak also appears broadened. One can see this broadening clearly by looking at the real part of the EXAFS data. In the first peak, the real part of the Cu EXAFS signal has a minimum where traces from all three particle sizes line up. However, the maxima on either side of this minimum are shifted from the center farther for the small particle data than the large or medium. There is also some structure farther out, $\sim 3-4\mathring{A}$, which while present in the large particle data set is completely washed out in the small particle data. Clearly there is something happening to the Cu environment when grinding takes place.

4.4 Implications of Results

We found that for ground ZnS:Cu,Mn,Cl separated by size, both the XANES and EXAFS did not change appreciably for the Zn (host) and Mn (dopant, $\sim 5\%$) edges, whereas significant changes occurred in the Cu (dopant, $\sim 0.15\%$) data.

The grinding must not be affecting a majority of the Zn host sites or Mn dopant sites because the EXAFS and XANES data for these edges are independent of reducing particle size. The grinding process must therefore affect the compound in such a way as to preserve the Zn and Mn structures. Earlier work in our lab showed that Mn resides on Zn sites in ZnS:Cu,Mn,Cl. This suggests why the Zn and Mn behave similarly—they are on the same sites, and so are affected by the grinding in the same way.

Although the Mn and Zn data are particle size independent, we found that this was not the case for the Cu data. Therefore, the grinding must be affecting the Cu sites in a manner different than how the grinding affects the Zn/Mn site. A plausible explanation relies on the way in which Cu is present in the ZnS:Cu,Mn,Cl.

The Cu is present in CuS needle-like precipitates [10] oriented along the (111) direction. With little strain, we have shown that two layers of CuS can be inserted into the ZnS:Cu,Mn,Cl lattice parallel to the (111) direction by removing three layers of the ZnS. However, doing so causes weak S-S bonds to form between the layers of CuS and ZnS:Cu,Mn,Cl, as well as within the CuS structure.

The S-S bonds seem like natural places for the crystal to cleave because the (111)

plane is a known cleavage plane for the zincblende ZnS structure [11]. Any sort of fracture along this plane would move Cu from an internal location closer to or even at the surface of the cleaved particle. Such a drastic change in the siting of the Cu must change the XANES and EXAFS. That is, because the Cu is no longer deep inside the particle, but near or on the surface, the EXAFS and XANES will be different, in agreement with our EXAFS and XANES results.

While we have been able to provide an explanation for why the EXAFS and XANES signals are particle-size dependent for only Cu and not Mn/Zn, we have yet to offer a reason why the EL is much reduced in the ground particle devices. It was shown [12, 10] that the EL for ZnS:Cu,Mn,Cl was directed along (111) directions, and that the needle-like CuS structures are important in device function.

When a voltage sine wave is applied to the device, the resultant electric field is thought to be enhanced at the tips of the needle-like CuS structures [10]. As the voltage oscillates, trapped hole and electron states accelerated by the enhanced field are alternatively filled. This drives the recombination of holes with electrons, producing light.

If the needle is completely internal to the particle, there will be trapped states completely surrounding it. However, if the ZnS:Cu,Mn,Cl is ground, causing cleavage to occur along the (111) direction across the boundary between ZnS and CuS, or within the CuS structure itself, the CuS needles are now exposed on the surface.

In the best case scenario, the CuS have half of the trap sites available to them before cleavage, because the needle is now on the surface. Depending on the curvature

of the fracture, the new number of available sites could be even fewer. This reduction in trap sites would inhibit light output; there simply are not enough opportunities for electrons to combine with holes and produce light when the particles are ground. Additionally, the presence of a dielectric material completely surrounding the CuS needles enhances the electric field compared to a needle surrounded by air. Thus cleavage not only reduces the number of states available to interact but also reduces the electric field strength.

Despite the overall result that ground particles made poorer devices, this is not entirely the case. In fact, particles slightly ground actually increased light output compared with unground particles. This can be explained by having recourse to the voltage/electric field across the CuS needle. That is, the electric field (E) and voltage (V) are proportional in this nearly perfectly capacitive device via the thickness of the device (d), yielding $V = Ed$. If the voltage is constant (as was done in our work), the product Ed must not change. Smaller particles imply a smaller d, and therefore the E-field must be larger to keep the voltage constant. The larger E-field now has enough strength to fill more electrons and hole trap states than when the particles were unground and the electric field smaller, and so the light output is greater.

Hence we see there are two competing effects of grinding on the light output of the devices. The grinding exposes the CuS structures and reduces significantly the number of trapped states available for recombination, inhibiting light output. However, grinding also reduces particle size and therefore device thickness, allowing for stronger E-fields and more light output for the same applied voltage. The interaction

of these two effects results in what we observe experimentally, namely that slight grinding provides a small boost in the light output, but excessive grinding reduces device output significantly. We see then that structural changes at the local level actively affect a macroscopic property of ZnS:Cu,Mn,Cl, namely its ability to EL.

5

$Ba_8Ga_{16}Sn_{30}$ EXAFS Studies

5.1 Background and Motivation

The type I clathrates $X_8Ga_{16}Ge_{30}$ (X=Ba, Sr, Eu)[13, 14] and recently $Ba_8Ga_{16}Sn_{30}$[15] have the unusual properties that the electrical conductivity σ is moderately good but the thermal conductivity κ is poor, nearly glass-like; consequently they come close to the electron-crystal/phonon-glass concept proposed by Slack[16] for good thermoelectric materials. These compounds are compensated semiconductors and for some systems the charge carrier type can be changed from n-type to p-type with a small variation in the Ga:Ge or Ga:Sn ratio. Unlike the type VIII clathrate form of $Ba_8Ga_{16}Sn_{30}$, which exhibits significant differences in the temperature dependence of the thermal conductivity between p- and n-type, the type I form considered here shows only a small difference in κ between p- and n-type[1]. However, κ for the n-type is consistently slightly larger than that found in the p-type.

The structure of the type I clathrates (X_8M_{46}) consists of two connected cages - a 20-atom cage (M20) and a 24-atom cage (M24). There are three crystallographic sites within this cage structure occupied by Ga/Ge or Ga/Sn atoms - M1 (6*c* site), M2 (16*i* site), and M3 (24*k* site). The X atoms are located near the centers of each of the two cages and it is believed that the low frequency "rattling" motion of X atoms, such as Eu and Sr, provides the main phonon scattering mechanism, but the coupling between the higher energy phonon vibrations in the cage structure and the X rattlers is more difficult to quantify. For $Ba_8Ga_{16}Ge_{30}$, the situation is less clear[17, 18] as in this clathrate the Ba2 offcenter displacement in the M24 cage is small,[17, 19] the results appear to be sample dependent, and disorder within the lattice cages may be important[17, 18]. However for $Ba_8Ga_{16}Sn_{30}$, considered here, Ba2 also has a large off-center displacement[1].

It has long been recognized that the distribution of Ga on the three sites is not random,[3, 20, 2] and the distribution may be important in determining the rattler-cage phonon coupling.[19] One suggestion is that the structure minimizes the number of Ga-Ga bonds - *i.e.* the group III element, Ga, prefers to have nearest neighbor Ge or Sn neighbors.[21, 3] Distributions of Ga on the three sites M1-M3 from diffraction are generally consistent with such a model[1, 20] but to date there is no direct proof.

This is where the strength of EXAFS enters. Because the spectra for the pair between a core element and another are unique, one can use EXAFS to tell whether the nearest neighbor to Ga is more likely Sn or Ga, and to what extent. The particular shape of the EXAFS signal varies with the atomic number of the nearest neighbor.

Since Ga and Sn differ in atomic number by 29, the Ga-Ga and Ga-Sn theorectical standards look significantly different (Fig. 5.1). This suggests that EXAFS can be used to clearly distinguish Ga and Sn neighbors in $Ba_8Ga_{16}Sn_{30}$.

5.2 Sample Preparation and Procedure

Single crystals were prepared by M. A. Avila *et al.*; see Refs. [15] and [1] for detailed information on the crystal growth. EXAFS samples were made by first grinding the crystals using a mortar and pestle and then passing the powder through a 400 mesh sieve. The resulting fine powder was brushed onto scotch tape. The tape preferentially holds the smaller grains ($\leq 5\mu$m) in a thin layer. Two layers of tape were pressed together (double layer) to encapsulate the powder. For the Ga K-edge measurements 4 double layers were used which gave Ga K-edge jumps of 0.4 (n-type) and 0.45 (p-type).

Note that for this compound, we ground the data and forced it through a sieve. This is the standard preparation method for our EXAFS samples, but was not done for the ZnS:Cu,Mn,Cl samples above because we were focusing there on the different sizes of the particles. Sifting the ZnS:Cu,Mn,Cl using a sieve would serve only to preferentially pick out the smallest particles and render our size separation useless.

The Ga K-edge EXAFS data were collected at SSRL (Stanford Synchrotron Radiation Lightsource) in transmission mode on beamline 10-2 using a Si 111 double monochromator. The slit height was 0.5 mm, which provided an energy resolution of

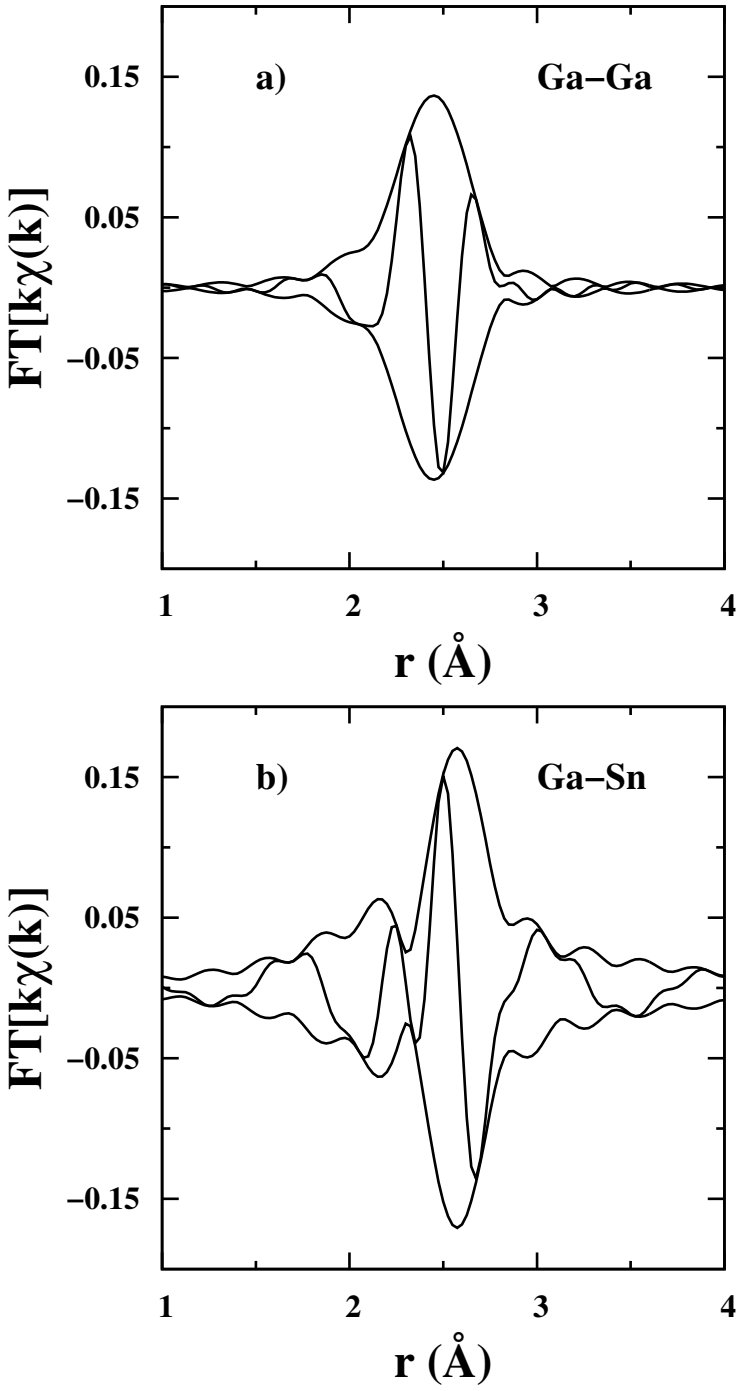

Figure 5.1: The theoretical r-space function for a) the Ga-Ga pair and b) the Ga-Sn pair calculated using FEFF. The FT range is 3.5-14.4 Å^{-1} with a Gaussian rounding of the FT window of 0.3 Å^{-1}. For both plots a small broadening ($\sigma^2 = 0.0020$ Å^2) was included and E_o was shifted to correspond to the E_o of the data.

$\sim$2 eV, and the monochromator was detuned 50% to minimize harmonics.

We studied the temperature dependence of the EXAFS signal for the Ga K-edge over a range of 4K to 300K. We used a resistor on the cryostat to serve as a heater and were able to regulate the temperature with a power regulator to within 1K.

5.3 EXAFS Results and Analysis

In Fig. 5.2, we show the raw data collected at SSRL for the Ga K-edge at 4K. After background subtraction and some data reduction explained above, we extracted the k- and r-space data, which we present in Fig. 5.3. Note how similar the r-space data and the Ga-Sn standard from Fig. 5.1 appear and how unlike the data and the Ga-Ga theoretical standard are. This visual comparison indicates that the majority of neighbors around Ga are Sn. Below through data fitting we reach quantitative results that confirm this conclusion.

We also varied the temperature of the sample and took EXAFS data as a function of temperature. For brevity, we show the r-space data only for the temperature-dependent EXAFS in Fig. 5.4. Note the overall reduction in amplitude as the temperature increases. This is typical of EXAFS signals and occurs because the pair distribution function (PDF) for each pair is broadened as the temperature (and therefore disorder) increases.

Since the data are so similar to the Ga-Sn function we started the fit with 75% Ga-Sn (*i.e.* 3 Sn neighbors) and 25% Ga-Ga. We allowed σ (width of the pair distribution

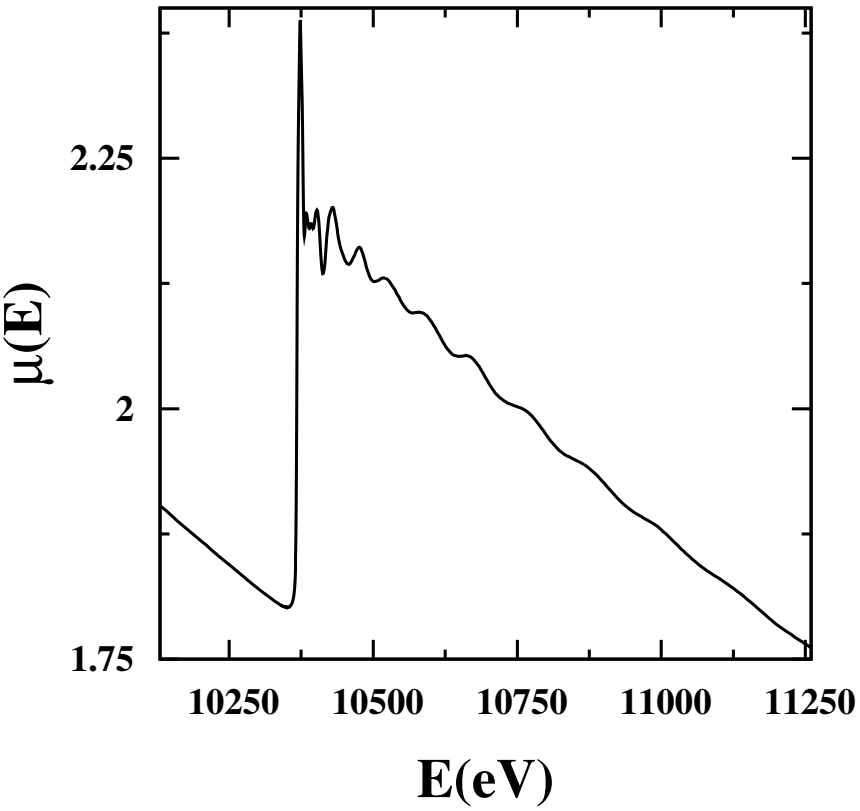

Figure 5.2: Raw data (energy space) for Ga K-edge $Ba_8Ga_{16}Sn_{30}$ n-type material at 4K.

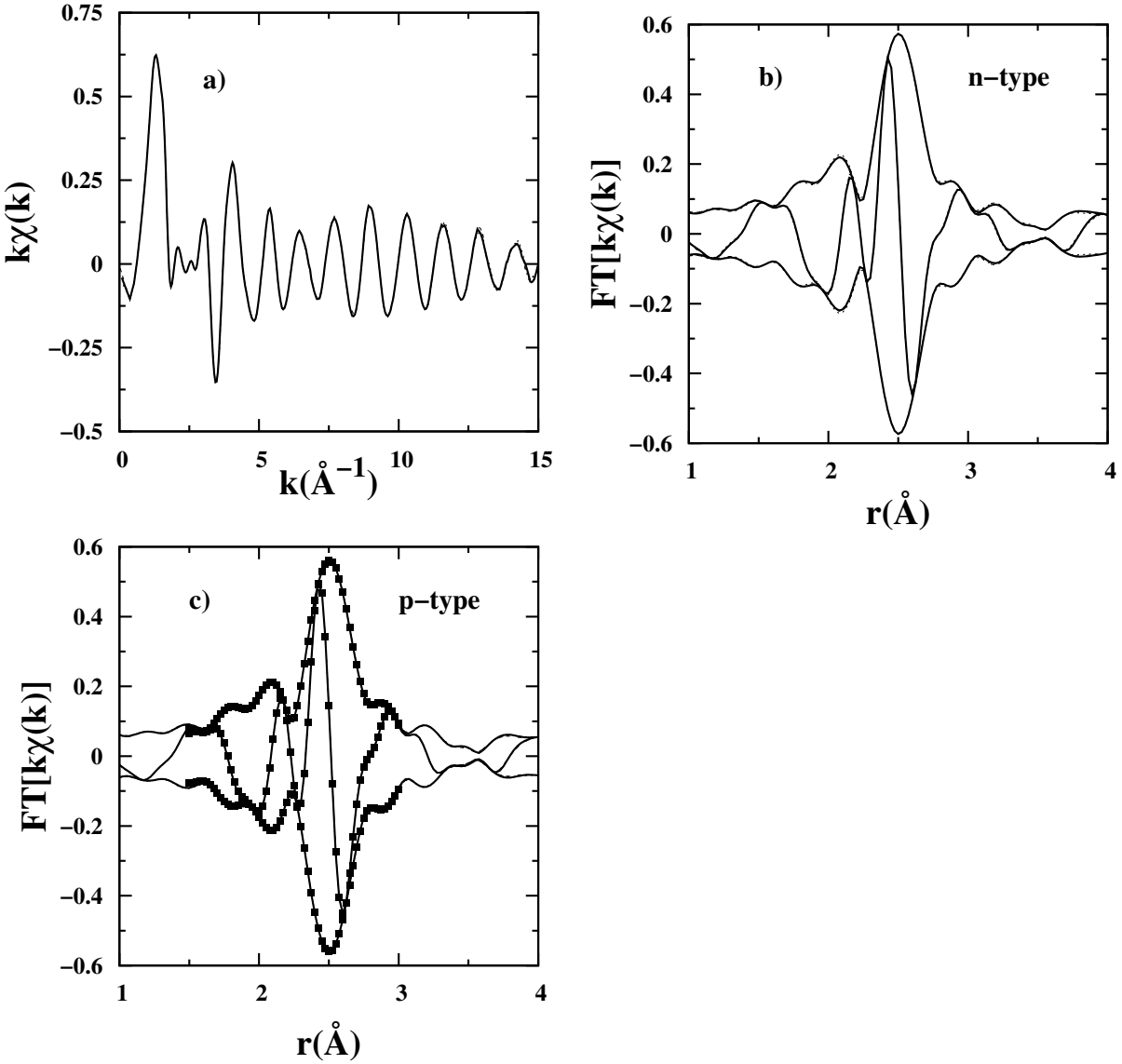

Figure 5.3: Ga K-edge data at 4K for $Ba_8Ga_{16}Sn_{30}$. a) k-space data, n-type; b) r-space data (n-type); c) r-space data (p-type) along with the fit from 1.5 to 3 Å (squares) [S_o^2 parameter is 0.93]. For each plot three traces are overlaid to show the high quality of the data—only above 14 Å in part a) can one see a tiny difference. Oscillations of r-space plots are the real parts of the Fourier transforms of $k * \chi(k)$ and the envelope functions represent the magnitude of the transform. The range of the Fourier transform is 3.5-14.4 Å.

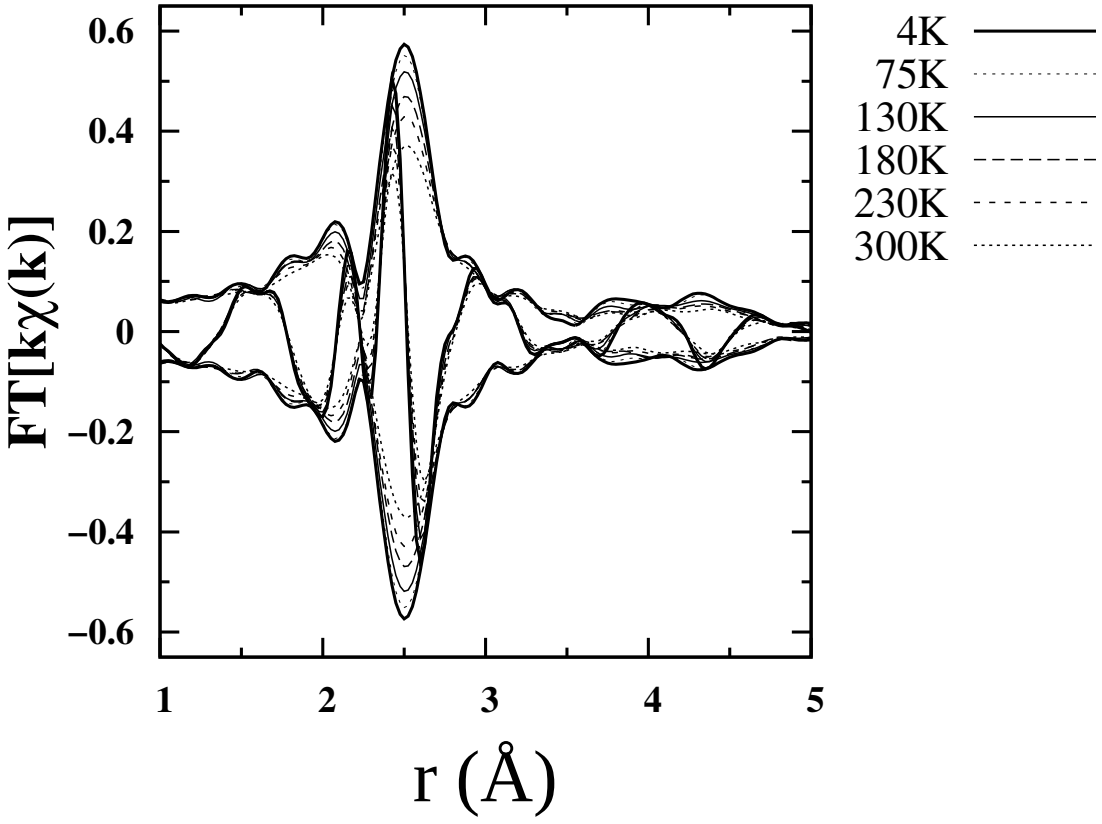

Figure 5.4: Temperture dependence of r-space data for Ga K-edge $Ba_8Ga_{16}Sn_{30}$ n-type.

function) and the bond length r of each pair to vary in the first fits. The fit range was from 1.5 to 3 Å in r-space and 3.5 to 14.4 $Å^{-1}$ in k-space. Note that the weak Ga-Ba1 peak occurs above 3.3Å, and does not contribute to this first peak.

Using further refinements to the fits, we find that in the n-type material 85% of the Ga neighbors are Sn and 15±5% are Ga (p-type identical), compared to 33% Ga nearest neighbors expected for a random distribution. These fits confirm the visual inspection of Figs. 5.1 and 5.3, namely that the Ga-Ga bonds make up only a small fraction of the nearest neighbor Ga bonds.

Our data suggest that there are either 4 or 5 Ga-Ga pairs in the unit cell, corresponding to 13% and 16% Ga-Ga respectively. Using these results in tandem with the occupational parameters measured by Suekuni *et al.*[1], we were able to construct one possible arrangement of the unit cell (Fig. 5.5) with 4 Ga-Ga pairs. Alternatively, by moving the Ga on site A in Fig. 5.5 to site B we leave the occupational parameters unchanged while adding one more pair of Ga atoms. Most likely there are other configurations as well since the asymmetry within the unit cell (while preserving translational symmetry at the surface) allows for several switches of Ga sites while not violating the occupational parameters.

Moreover, from the fits, we found both the Ga-Ga and Ga-Sn bond lengths are shorter than the averages calculated using the crystal structure.[15] We started the fit with the average Ga-Ga and Ga-Sn bond length, each 2.73 Å, but the two shifted down to 2.55 Å and 2.66 Å (n-type), and 2.54 Å and 2.66 Å (p-type), respectively. It is of interest that the Ga-Ga bond shifts down to approximately 2.55 Å, almost

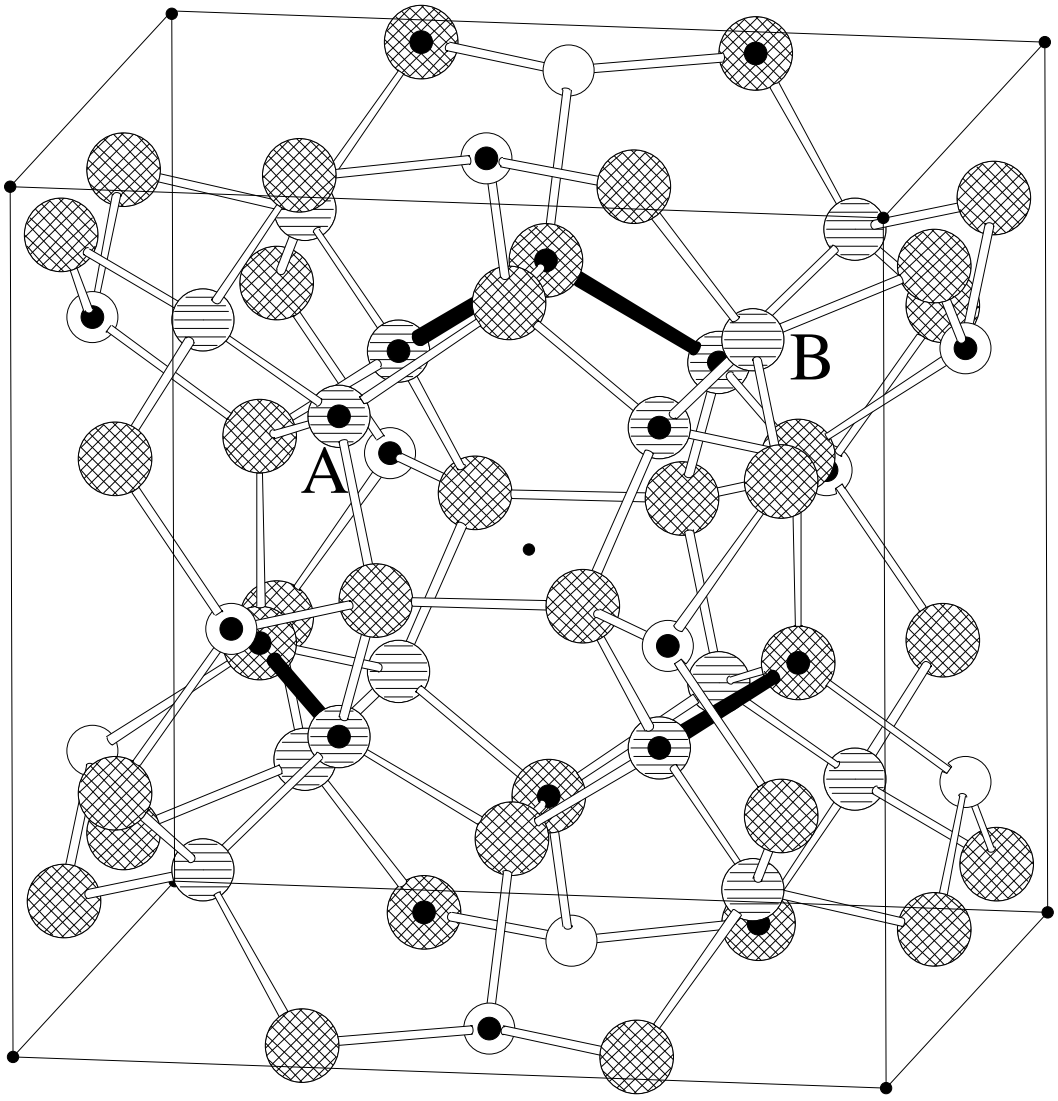

Figure 5.5: The unit cell of $Ba_8Ga_{16}Sn_{30}$. The small black dots on the corners and in the center are the Ba1 sites. The Ba2 sites are removed for clarity. The largest balls (cross-hatches) are the M3 ($24k$) sites. The medium balls (horizontal stripes) are the M2 ($16i$) sites. The small balls (no texture) are the M1 ($6c$) sites. A site occupied by Ga is marked by a black dot in the center of one of the larger balls. The four Ga-Ga bonds are in black. Site B is an alternate location for the Ga at A; switching these yields one more Ga-Ga pair.

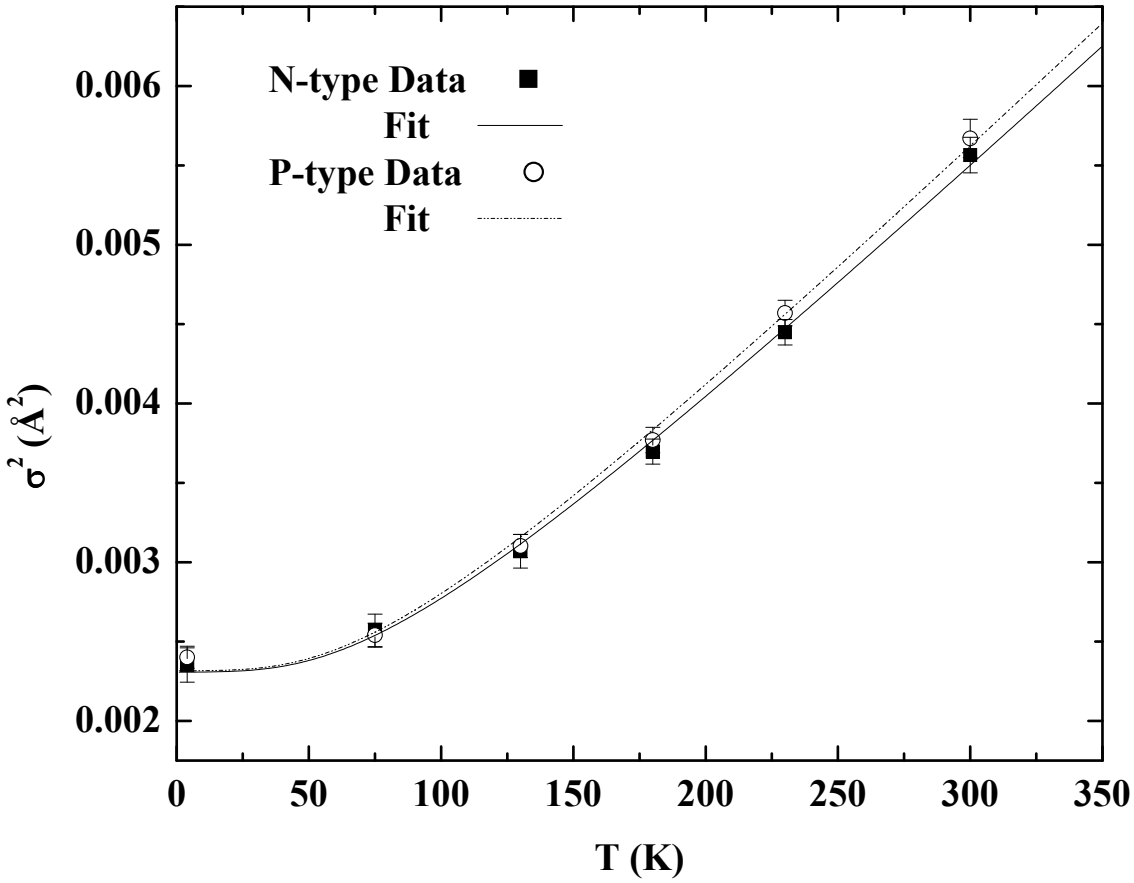

Figure 5.6: Temperature dependence of σ^2 for the Ga-Sn bond with a fit to a correlated Debye model. The n-type data are shown as solid squares with fit the solid line; the p-type data are represented by the empty circles and the fit by the dashed line.

0.2 Å below the average bond length, and closer to the Ga-Ga/Ge bond distances in $Ba_8Ga_{16}Ge_{30}$ (2.50 Å on average).[22, 19] This indicates that the Ga-Ga bond length is roughly constant regardless of the other cage atom.

The shorter Ga-Sn and Ga-Ga bonds here also imply that the Sn-Sn distance should be larger than the average bond distance. A preliminary check of one Sn K-edge scan is consistent with a larger Sn-Sn bond, but more data are needed.

We fit σ^2 of the Ga-Sn first neighbor bond to a correlated Debye model (see Fig. 5.6), and found the correlated Debye temperature to be 315±20K for the n-type

Table 5.1: Fractional occupational parameters of the Ga atom for several type I clathrates. Note a =Ref. [1], b = Ref. [2], c = Ref. [3].

Compound	Method	$6c$	$16i$	$24k$
$Ba_8Ga_{16}Sn_{30}$ (n-type)^a	x-ray	0.71	0.36	0.25
$Ba_8Ga_{16}Sn_{30}$ (p-type)^a	x-ray	0.68	0.34	0.26
$Ba_8Ga_{14.6}Si_{31.4}{}^b$	x-ray	0.61	0.08	0.40
$Ba_8Ga_{15.7}Si_{30.3}{}^b$	neutron	0.63	0.11	0.43
$Ba_8Ga_{16}Ge_{30}$ (n-type)^c	x-ray	0.76	0.16	0.37
$Ba_8Ga_{16}Ge_{30}$ (n-type)^c	neutron	0.74	0.17	0.37
$Ba_8Ga_{16}Ge_{30}$ (p-type)^c	x-ray	0.64	0.17	0.39
$Ba_8Ga_{16}Ge_{30}$ (p-type)^c	neutron	0.60	0.33	0.30

Table 5.2: Fractional occupational parameters of the Ga atom for several type I clathrates. Note a =Ref. [1], b = Ref. [2], c = Ref. [3].

material and 310±20K for the p-type, essentially the same within our errors.

Note that our EXAFS data apply only to $Ba_8Ga_{16}Sn_{30}$; however, the fractional occupational parameters of other type I clathrates containing Ga are roughly similar (see Table 5.2), though the variation is large especially for the $16i$ and $24k$ sites. It seems reasonable, then, to expect the Ga-Ga bonds to be likewise suppressed in other clathrates, even if the actual number of Ga-Ga bonds varies slightly, but it needs to be checked.

5.4 Implications of Results

We found that the number of Ga-Ga bonds was fewer than randomness would predict ($\sim$ 15% instead of 33%). This is a direct confirmation of Blake *et al.*'s[21] prediction that the lowest energy configuration has few Ga-Ga pairs. However, having some Ga-Ga pairs as our data suggest is not the lowest energy configuration; there are configurations where Ga-Ga pairs are nonexistent. That our data show there are Ga-Ga bonds suggests that there may be something missing in the calculations for the energies of the various bond configurations.

Additionally, we found that both the Ga-Ga and Ga-Sn distances were shorter than the average bond distance, and a check of Sn edge data revealed the Sn-Sn distance to be longer. The magnitude of these deviations from the average bond length indicates that the $Ba_8Ga_{16}Sn_{30}$ cage structure is significantly disordered; it also suggests that the cages might be dimpled.

The correlated Debye temperatures we found for the n- and p-type $Ba_8Ga_{16}Sn_{30}$ are smaller than those found in $Ba_8Ga_{16}Ge_{30}$ for the Ga-Ga/Ge bond, namely 410K and 415K (n-type and p-type respectively).[19] This suggests the Ga-Sn bond is weaker than the average Ga-Ga/Ge bond.

The disorder of the $Ba_8Ga_{16}Sn_{30}$ structure helps to explain the lower thermal conductivity exhibited by this clathrate compared to similar compounds.[1] Part of the reason that $Ba_8Ga_{16}Sn_{30}$ is a reasonable thermoelectric is because of its low thermal conductivity. While the lower thermal conductivity can be explained in part by

the scattering of low frequency phonons off the rattling caged Ba atoms, the highly disordered cage structure we discovered must also contribute to the low thermal conductivity. Unfortunately, $Ba_8Ga_{16}Sn_{30}$ also has a lower electrical conductivity (and so its thermoelectric figure of merit is less than unity [23, 1]), likely as a consequence of this disordered cage structure. Thus, we see that it is the local structure of $Ba_8Ga_{16}Sn_{30}$ that helps explain some of its global properties—the thermal and electrical conductivities.

It should be noted that these results have been recently published in Physical Review B [24].

6

Conclusion

There is a recurrent theme in our EXAFS studies. We examine materials with novel properties using EXAFS. However, EXAFS only explicitly reveals the local structure of the materials. It does not directly describe the macroscopic characteristics of different compounds. However, we are able to use the information provided by the local structure to explain (at least in part) certain global properties of interesting materials.

Above we showed that for small particle sizes produced through grinding Cu K-edge EXAFS (and XANES) were significantly different for different sized particles, whereas the Zn and Mn K-edge data remained unchanged. Using this fact, we were able to provide a possible reason why EL devices made from small ground particles are typically less effective. Namely, by grinding the material we are likely cleaving along the boundary between ZnS and embedded CuS needles (where EL occurs), bringing the Cu needles to the surface and reducing the number of trapped states available for

recombination and light output.

Moreover, we showed that the cage structure of $Ba_8Ga_{16}Sn_{30}$, a thermoelectric material, was more disordered than suggested in diffraction data. The Ga-Sn and Ga-Ga bond lengths were signifcantly shorter than the average bond length, and a quick check of Sn edge data revealed that the Sn-Sn bond was longer than average (though more data are necessary here). This disorder—a local property—must contribute to the low thermal conductivity—a global property—exhibited by this compound.

Hence, the power of EXAFS is not simply its ability to describe local structure. Rather, it is the ability of EXAFS studies to reveal aspects of local structure that explain global properties that makes the technique remarkably useful.

Bibliography

[1] K. Suekuni, M. A. Avila, K. Umeo, H. Fukuoka, S. Yamanaka, T. Nakagawa, and T. Takabatake, Phys. Rev. B **77**, 235119 (2008).

[2] A. Bentien, E. Nishibori, S. Paschen, and B. B. Iversen, Phys. Rev. B **71**, 144107 (2005).

[3] M. Christensen and B. B. Iversen, Chem. Mater. **19**, 4896 (2007).

[4] B. K. Teo, EXAFS: Basic Principles and Data Analysis (Springer-Verlag, New York, 1986).

[5] S. I. Zabinsky, J. J. Rehr, A. Ankudinov, R. C. Albers, and M. J. Eller, Phys. Rev. B **52**, 2995 (1995).

[6] C. H. Booth, R-Space X-ray Absorption Package, http://lise.lbl.gov/RSXAP/.

[7] S. Tanaka, H. Kobayashi, and H. Sasakura, in Phosphor Handbook, edited by S. Shionoya and W. Yen (CRC Press, New York, 1999), Chap. 9, pp. 601–612.

[8] M. Warkentin, F. Bridges, S. A. Carter, and M. Anderson, Phys. Rev. B **75**, 075301/1 (2007).

[9] K. Lu and E. Stern, Nucl. Instrum. Methods **212**, 475 (1982).

[10] A. Fischer, J. Electrochem. Soc. **110**, 733 (1963).

[11] W. H. Bragg and W. L. Bragg, Nature **91**, 557 (1913).

[12] A. Fischer, J. Electrochem. Soc. **109**, 1043 (1962).

[13] B. C. Sales, B. C. Chakoumakos, R. Jin, J. R. Thompson, and D. Mandrus, Phys. Rev. B **63**, 245113(1) (2001).

[14] G. S. Nolas, J. L. Cohn, G. A. Slack, and S. B. Schujman, Appl. Phys. Lett **73**, 178 (1998).

[15] M. A. Avila, K. Suekuni, K. Umeo, H. Fukuoka, S. Yamanaka, and T. Takabatake, Applied Physics Letters **92**, 041901 (2008).

[16] G. A. Slack, in CRC Handbook of Thermoelectrics, edited by D. M. Rowe (Chemical Rubber, Boca Raton, FL, 1995), pp. 407–440.

[17] M. Christensen, N. Lock, J. Overgaard, and B. B. Iverson, J. Am. Chem. Soc. **128**, 15657 (2006).

[18] M. Christensen, A. B. Abrahamsen, N. B. Christensen, F. Juranyi, N. H. Anderson, K. Lefmann, J. Andreasson, C. R. H. Bahl, and B. B. Iverson, Nat. Mater. **7**, 811 (2008).

[19] Y. Jiang, F. Bridges, M. A. Avila, T. Takabatake, J. Guzman, and G. Kurczveil, Phys. Rev. B **78**, 014111 (2008).

[20] Y. Zhang, P. Lee, G. Nolas, and A. Wilkinson, Appl. Phys. Lett. **80**, 2931 (2002).

[21] N. P. Blake, D. Bryan, S. Latturner, L. Mollnitz, G. D. Stucky, and H. Metiu, Journal of Chemical Physics **114**, 10063 (2001).

[22] B. C. Chakoumakos, B. C. Sales, and D. G. Mandrus, Journal of Alloys and Compounds **322**, 127 (2001).

[23] M. Hayashi, K. Kishimoto, K. Akai, H. Asada, and T. Koyanagi, Dalton Trans. **39**, 1113 (2010).

[24] M. Kozina, F. Bridges, Y. Jiang, M. A. Avila, K. Suekuni, and T. Takabatake, Phys. Rev. B **80**, 212101 (2009).